RSC Advances

ROYAL SOCIETY OF CHEMISTRY

PAPER

View Article Online
View Journal | View Issue

Cite this: *RSC Adv.*, 2024, **14**, 24031

Facile synthesis of MnO/NC nanohybrids toward high-efficiency ORR for zinc–air battery†

Qingxi Zhuang,‡[a] Chengjun Hu,‡[a] Weiting Zhu,[a] Gao Cheng,*[a] Meijie Chen,[a] Ziyuan Wang,[b] Shijing Cai,[b] Litu Li,[a] Zier Jin*[b] and Qiang Wang*[c]

The development of inexpensive non-precious metal materials as high-efficiency stable oxygen reduction reaction (ORR) catalysts holds significant promise for application in metal–air batteries. Here, we synthesized a series of nanohybrids formed from MnO nanoparticles anchored on N-doped Ketjenblack carbon (MnO/NC) *via* a facile hydrothermal reaction and pyrolysis strategy. We systematically investigated the influence of pyrolysis temperature (600 to 900 °C) on the ORR activities of the MnO/NC samples. At the optimized pyrolysis temperature of 900 °C, the resulting MnO/NC (referred to as MnO/NC-900) exhibited superior ORR activity (onset potential = 0.85 V; half-wave potential = 0.74 V), surpassing other MnO/NC samples and nitrogen-doped Ketjenblack carbon (NC). Additionally, MnO/NC-900 demonstrated better stability than the Pt/C catalyst. The enhanced ORR activity of MnO/NC-900 was attributed to the synergy effect between MnO and NC, abundant surface carbon defects and surface-active components (N species and oxygen vacancies). Notably, the Zinc–air battery (ZAB) equipped MnO/NC-900 as the cathode catalyst delivered promising performance metrics, including a high peak power density of 146.5 mW cm^{-2}, a large specific capacity of 795 mA h g_{Zn}^{-1}, and an excellent cyclability up to 360 cycles. These results underscore the potential of this nanohybrid for applications in energy storage devices.

Received 10th June 2024
Accepted 19th July 2024

DOI: 10.1039/d4ra04237a

rsc.li/rsc-advances

1. Introduction

High-efficiency and stable electrocatalysts for the oxygen reduction reaction (ORR) are vital for advancing metal–air batteries.[1–4] While Pt-based electrocatalysts are widely utilized, their high cost and poor stability impede broader adoption.[5,6] Extensive research has focused on developing non-precious metal catalysts with robust stability.[7–10] Recently, transition metal oxides have drawn increasing research interests as ORR electrocatalysts.[11–13] Amongst the categories, manganese oxides (MnO_x, *e.g.*, MnO, Mn_3O_4, and MnO_2) gradually emerged as promising candidates due to their eco-friendliness, affordability, tunable crystalline phases, and unique redox properties.[14–16] However, standalone manganese oxides often exhibit inadequate ORR activities due to their low conductivity, limited active sites, and nanoparticle aggregation during ORR.[17]

To address these challenges, dispersing MnO_x nanostructures (MONs) on carbon-based substrates, such as graphene, hollow carbon, and three-dimensional (3D) carbon, has emerged as a popular strategy to enhance conductivity and prevent aggregation.[18–22] For instance, Wang *et al.* presented a ε-MnO_2/reduced graphene oxide sheet-like nanohybrid, which exhibited better ORR properties compared to the reduced graphene oxide.[19] Wu *et al.* reported a nanocomposite catalyst that integrated MnO_2 nanofilms with N-doped hollow graphene spheres (MnO_2/N-HGSs).[20] The assembled solid-state ZAB with MnO_2/N-HGSs cathode achieved a large power density of 82 mW cm^{-2} and specific capacity of 744 mA h g_{Zn}^{-1}. Gao *et al.* synthesized a MnO/3D N-doped carbon nanohybrid *via* a two-step pyrolysis route, demonstrating exceptional ORR activity and durability.[21] However, the above carbon-based substrates were high cost or required multistep synthetic procedures. Amongst all the carbon-based substrates, commercial carbon nanoparticles (CCNs), such as Carbot Vulcan and Ketjenblack, have many advantages, *e.g.*, low price, easily available, large surface area, and remarkable conductivity. These merits make CCNs an ideal carrier for supporting nanostructured ORR electrocatalysts.[23–27] For instance, the Cu/CuO_x-Co_3O_4/NC nanohybrid fabricated *via* a two-step hydrothermal-calcination method demonstrated outstanding specific capacity in zinc–air batteries.[23] Additionally, cubic-$CoMn_2O_4$/Carbot Vulcan nanocomposite exhibited ORR activity comparable to the Pt/C

[a]*School of Chemical Engineering and Light Industry, Guangdong University of Technology, Guangzhou 510006, China. E-mail: chengg36@gdut.edu.cn*

[b]*Foshan Institute of Environment and Energy Technology, Foshan 528000, China. E-mail: fieet0325@163.com*

[c]*School of Materials and Energy, Chongqing Key Lab for Battery Materials and Technologies, Southwest University, Chongqing 400715, China. E-mail: wysnu@swu.edu.cn*

† Electronic supplementary information (ESI) available. See DOI: https://doi.org/10.1039/d4ra04237a

‡ These authors contributed equally to this work.

catalyst.[26] Thus, engineering MONs/CCNs nanohybrids holds promise for enhancing the performance of metal–air batteries.

Motivated by these insights, in this study, we developed Mn-based nanohybrids of MnO nanoparticles loaded on N-doped Ketjenblack carbon (MnO/NC) through a facile synthetic strategy. The $MnCO_3$ anchored on NC precursor was first synthesized using a hydrothermal method, followed by pyrolysis to form a MnO/NC nanohybrid. We discussed the effect of calcination temperature on the ORR activities of MnO/NC samples, highlighting the optimized sample (pyrolysis temperature: 900 °C) with outstanding ORR activity and durability in alkaline media. Furthermore, as a cathode electrocatalyst for ZAB, this sample demonstrated high-efficiency ZAB performance, suggesting its promising application in metal–air batteries.

2. Experimental section

2.1. Materials

Manganese(II) acetate tetrahydrate ($Mn(CH_3COO)_2\cdot 4H_2O$, 99.0%), zinc(II) acetate dihydrate ($Zn(CH_3COO)_2\cdot 2H_2O$, 99.0%), urea ($CO(NH_2)_2$, 99.5%), and nitric acid (HNO_3, 65–68%) were procured from Guangzhou Chemical Reagent Factory. Potassium hydroxide (KOH, 99.999%) was acquired from Aladdin Reagent (Shanghai) Co., Ltd. Ketjenblack carbon was sourced from Japan Lion Ltd (EC 600JD). Pt/C (20 wt%) was acquired from Johnson Matthey Chemicals Ltd.

2.2. Synthesis of MnO/NC nanohybrids

Before utilization, Ketjenblack carbon (KC) nanoparticles underwent initial pretreatment in an HNO_3 solution, following our previously published procedures.[28] Typically, the MnO/NC nanohybrid was synthesized in two sequential steps: (1) in a hydrothermal reaction, 10 mg of $Mn(CH_3COO)_2\cdot 4H_2O$, 100 mg of $CO(NH_2)_2$, and 70 mg of KC were added to 15 mL deionized water and stirred for ~30 min. The resulting suspension was then transferred to a Teflon-lined autoclave (25 mL) for hydrothermal reaction at 140 °C for 12 h. The resulting precursor was washed with deionized water and alcohol, and dried overnight at 60 °C. (2) Following the hydrothermal step, the precursor was subjected to high-temperature calcination. It was annealed at 900 °C for 2 h under an air atmosphere, resulting in the final MnO/NC nanohybrid (named as MnO/NC-900). Additionally, pure N-doped KC was obtained using the same synthesis process without adding $Mn(CH_3COO)_2\cdot 4H_2O$, designated as NC-900.

Controlled experiments were conducted with various calcination temperatures (600, 700, and 800 °C) for the precursor to optimize the electrocatalytic performance of the MnO/NC nanohybrids. These products were labeled as MnO/NC-600, MnO/NC-700, and MnO/NC-800, respectively.

2.3. Characterizations

The samples underwent comprehensive characterization using various techniques, including X-ray diffraction (XRD) analysis, field-emission scanning electron microscopy (FESEM), X-ray photoelectron spectroscopy (XPS), among others. Specific details and measured parameters of the instruments used are provided in the ESI.†

3. Results and discussion

Fig. 1a illustrates the synthetic pathway for MnO/NC nanohybrids, prepared through a combination of hydrothermal and post-pyrolysis methods. XRD analysis was employed to determine the crystal phase of all samples. Fig. S1† displays the XRD pattern of the precursor, revealing six peaks at 24.0°, 31.2°, 37.4°, 41.3°, 44.9°, and 51.2°, corresponding to (012), (104), (110), (113), (202), and (116) planes of rhombohedral $R\bar{3}c$ $MnCO_3$ (PDF# 44-1472). Additionally, a broad peak at ~22.5° indicates the presence of graphitic carbon (002),[29] suggesting the formation of a hybrid material comprising $MnCO_3$ and NC. Fig. 1b presents the XRD patterns of the final products obtained after calcination at various temperatures (600–900 °C). Five diffraction peaks at 34.8°, 40.5°, 58.4°, 69.9°, and 73.6° correspond to the (111), (200), (220), (311), and (222) planes of cubic $Fm\bar{3}m$ MnO (PDF# 75-1090), indicating the conversion of $MnCO_3$ into MnO through pyrolysis.

Raman spectroscopy was used to assess the degree of surface defects in carbon support after calcination at different temperatures. The Raman spectra (Fig. 1c) reveal the presence of a defect band (D-band) at ~1335 cm^{-1} and a graphite layer (G-band) at ~1591 cm^{-1} for all MnO/NC samples. The I_D/I_G ratio increases with higher calcination temperatures, with MnO/NC-900 (1.38) > MnO/NC-800 (1.36) > MnO/NC-700 (1.28) > MnO/NC-600 (1.25), indicating enhanced surface carbon defects with increasing temperature. These results suggest that MnO/NC-900, with more surface carbon defects, might exhibit improved ORR performance.[30]

FESEM was used to characterize the shapes of all MnO/NC samples (Fig. 2a–d), revealing nanoparticle-like shapes with an average diameter of ~50 nm. Further microstructural analysis of MnO/NC-900 using FETEM confirms the homogeneous

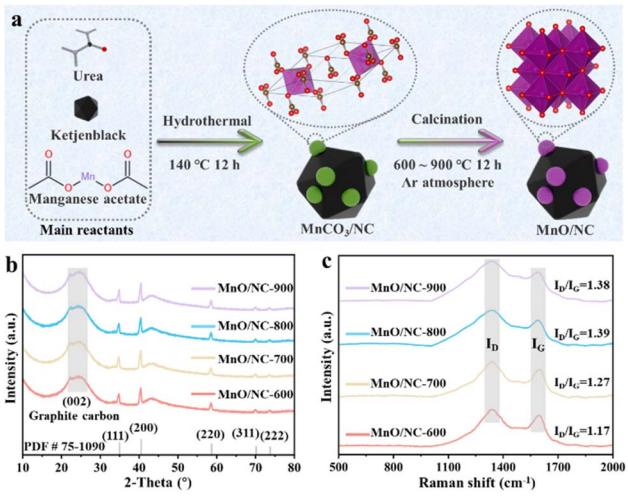

Fig. 1 (a) Schematic of the synthetic route to MnO/NC nanohybrids. (b) XRD patterns and (c) Raman spectra of MnO/NC nanohybrids.

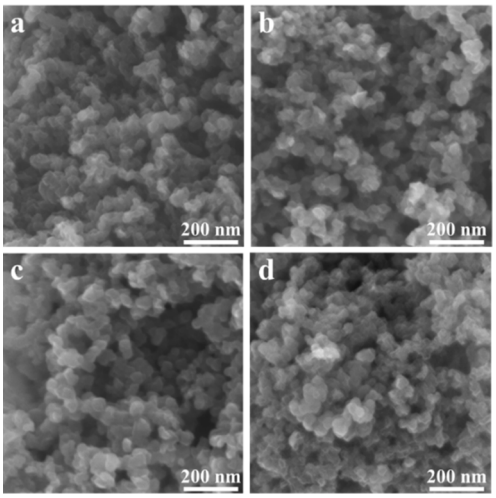

Fig. 2 FESEM images of (a) MnO/NC-600, (b) MnO/NC-700, (c) MnO/NC-800, and (d) MnO/NC-900.

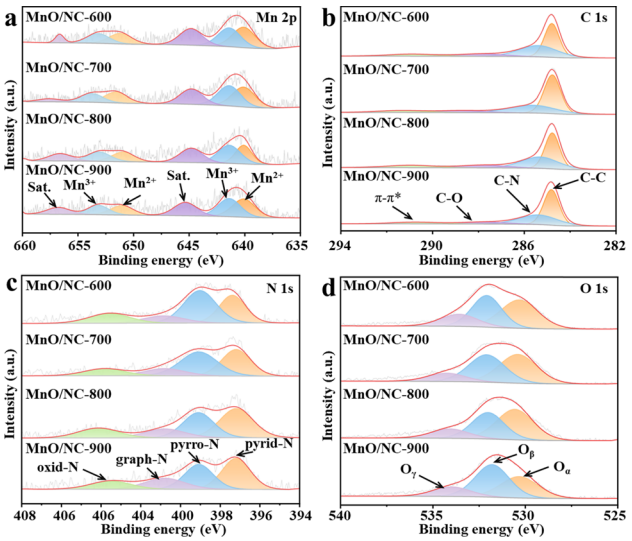

Fig. 4 High-resolution XPS spectra of MnO-NC nanohybrids: (a) Mn 2p, (b) C 1s, (c) N 1s, and (d) O 1s.

deposition of MnO nanoparticles on the NC surface (Fig. 3a), with a mean nanoparticle size of 15.6 nm (Fig. S2†). High-resolution FETEM image (Fig. 3b) demonstrates a *d*-spacing of 0.256 nm, consistent with the (111) plane of MnO, and a *d*-spacing of 0.330 nm, corresponding to the graphite carbon (002) plane. The carbon support plays a crucial role in preventing MnO nanoparticles agglomeration, which is conducive to maintaining the high ORR stability for the MnO/NC nanohybrids.[31]

The composition and bonding characteristics of all samples were further elucidated using XPS. In the wide XPS spectra (Fig. S3†), four peaks attributed to C 1s, N 1s, O 1s, and Mn 2p are observed, confirming the presence of C, N, O, and Mn elements in all samples. Additionally, the total amounts of Mn, N, and O elements are summarized in Table S1.† The Mn 2p spectra (Fig. 4a) demonstrate the existence of Mn^{2+} (640.2/651.6 eV) and Mn^{3+} (642.7/654.0 eV), matching well with those of reported MnO-based nanocomposites.[32] This Mn 2p result reveals that Mn^{2+} and Mn^{3+} species both existed in MnO for all the nanohybrids. Moreover, a satellite peak at 640.2 eV further demonstrates the presence of MnO.[33] Fig. 4b shows the C 1 s spectra, which are well deconvoluted into four peaks. That is, four types of C species exist in NC for all the samples. According to the literature,[34,35] the peaks at 284.8, 285.4, 287.6, and 290.8 eV are ascribed to C–C, C–N, C–O, and π–π*, respectively. The presence of C–N verifies that N atoms were successfully doped into the carbon substrate. The doped N atoms were derived from urea hydrolysis during the hydrothermal reaction.

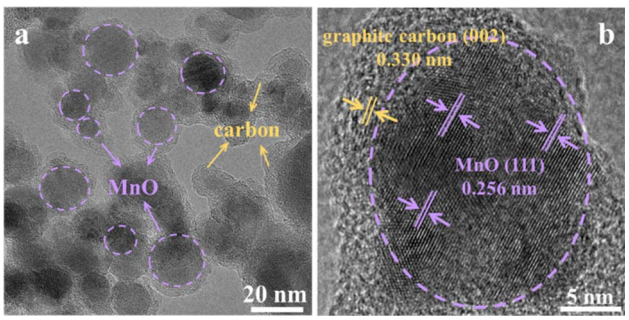

Fig. 3 (a) FETEM and (b) HR-FETEM images of MnO/NC-900.

The high-resolution spectra for the N 1s region (Fig. 4c) reveal four types of N species: pyridinic-N (397.2 eV), pyrrolic-N (399.1 eV), graphitic-N (400.8 eV), and oxidized-N (403.5 eV).[36,37] Results from Table S2† indicate that the calcination temperature significantly influences the content of N species. Notably, the content of pyrrolic-N gradually decreases with increasing temperature. As the temperature rises, pyrrolic-N is converted to graphitic-N and pyridinic-N, consistent with previous studies.[38,39] Consequently, the contents of pyridinic-N and graphitic-N follow the order: MnO/NC-900 > MnO/NC-800 > MnO/NC-700 > MnO/NC-600. Pyridinic-N and graphitic-N play crucial roles in enhancing the ORR activities of electrocatalysts due to the following aspects: (a) pyridinic-N could activate adjacent C atoms as the potential reactive sites for ORR;[40,41] (b) graphite-N is an excellent electron carrier, which could boost the adsorption rate of oxygen under the ORR process.[42,43] The O 1s spectra (Fig. 4d) exhibit three distinct peaks labeled as O_α, O_β, and O_γ, centered at 530.3, 531.8, and 534.0 eV, respectively. These peaks correspond to metal–oxygen, surface oxygen vacancy, and surface adsorbed –OH, respectively.[44] The relative proportions of O_β, calculated based on the O_β peak area (Table S3†), show the trend: MnO/NC-900 > MnO/NC-800 > MnO/NC-700 > MnO/NC-600. Generally, increased surface oxygen vacancies enhance the hydrophilicity of the electrocatalyst, facilitating the three-phase interface reaction for ORR.[45,46]

To evaluate the ORR performance of all synthesized samples, cyclic voltammetry (CV) test was initially conducted in O_2-saturated KOH solution (0.1 M). As depicted in Fig. S4,† the reduction peak position for MnO/NC-900 is observed at 0.75 V, which is higher than that of other MnO/NC samples and NC-

900. The more positive peak potential of MnO/NC-900 indicates its enhanced ORR performance. Subsequently, linear sweep voltammetry (LSV) of all samples at 1600 rpm were measured using a rotating disk electrode (RDE). Noticeably, MnO/NC-900 exhibits preferable onset potential (E_{onset} = 0.85 V) and half-wave potential ($E_{1/2}$ = 0.74 V), which are much more positive than those of MnO/NC-800, MnO/NC-700, MnO/NC-600, and NC-900 (Fig. 5a and b), and even exceed the $E_{1/2}$ values of many reported Mn-based catalysts (Table S4†). Furthermore, the limiting current density (J_L) at MnO/NC-900 (5.89 mA cm^{-2}) is substantially higher than that at MnO/NC-800 (4.97 mA cm^{-2}), MnO/NC-700 (4.99 mA cm^{-2}), MnO/NC-600 (4.43 mA cm^{-2}), and NC-900 (4.72 mA cm^{-2}). The Pt/C catalyst was also employed as the reference sample. As presented in Fig. S5,† the J_L of MnO/NC-900 is close to that of Pt/C. The ORR kinetics for all samples were also evaluated by the corresponding Tafel slopes (Fig. 5c). As expected, the MnO/NC-900 sample exhibits the smallest Tafel slope of 90.5 mV dec^{-1}, indicating its fastest electrocatalytic kinetics. These findings demonstrate the significant role played by both MnO and NC in synergistically enhancing the ORR activities of MnO/NC nanohybrids.

LSV curves were conducted at various rotating speeds (400–2500 rpm) to investigate the electron transfer mechanism. Clearly, the current density increases with higher rotational speed (Fig. S6†). In Fig. 5d, the Koutecky–Levich (K–L) curves show excellent linearity for both MnO/NC-900 and Pt/C. Furthermore, the K–L curve of MnO/NC-900 exhibits a slope quite similar to that of Pt/C, suggesting that MnO/NC-900 undergoes a quasi-4e$^-$ ORR mechanism. The rotating ring-disk electrode (RRDE) technique was additionally employed to understand the ORR process. Fig. S7† presents the corresponding LSV curves obtained from the RRDE. The calculated values of H_2O_2 yield and electron transfer number (n) are depicted in Fig. 5e. From 0.69 to 0.78 V, the H_2O_2 yield of MnO/NC-900 (~14.6%) is much lower than the other samples, again confirming its enhanced ORR performance. Furthermore, the corresponding n values for MnO/NC-900, MnO/NC-800, MnO/NC-700, MnO/NC-600, and NC-900 are 3.71, 3.49, 3.30, 3.33, and 2.81, respectively, verifying the quasi-4e$^-$ pathway of MnO/NC-900. Besides, the stabilities of MnO/NC-900 and Pt/C were evaluated using chronoamperometry (i–t). As depicted in Fig. 5f, a noticeable current change of 22.0% is observed for Pt/C after a 10 h test. In contrast, only a minor current decrease of 7.5% is noted for MnO/NC-900, indicating its superior stability. This suggests a protective effect of the carbon support on the MnO nanoparticles during the ORR process.

The aforementioned ORR results suggest that the MnO/NC-900 nanohybrid demonstrates outstanding electrocatalytic performance and durability. This is likely attributed to the optimal hybrid structure of MnO/NC-900, along with abundant electrocatalytically active sites (EASs), such as surface carbon defects and surface-active components (pyridinic- and graphitic- nitrogen species and oxygen vacancies). Generally, the EASs number of electrocatalysts can be reflected by its electrochemical surface area (ECSA), which is linearly correlated with the double-layer capacitance (C_{dl}) from CV tests at diverse rotational speeds (Fig. S8†). As revealed in Fig. S9,† MnO/NC-900 has a larger C_{dl} value (14.2 mF cm^{-2}) compared with MnO/NC-800 (9.5 mF cm^{-2}), MnO/NC-700 (11.2 mF cm^{-2}), and MnO/NC-600 (11.5 mF cm^{-2}). This indicates that MnO/NC-900 possesses the most EASs among all the MnO/NC nanohybrids, leading to its superior ORR activity.

Motivated by its promising ORR activity, we utilized the MnO/NC-900 catalyst as the air cathode for an aqueous alkaline ZAB denoted as MnO/NC-900-ZAB. Fig. S10† illustrates the schematic model of an aqueous alkaline ZAB, with a zinc plate serving as the anode and a mixed solution (0.2 M $Zn(AC)_2$ + 6 M KOH) as the electrolyte. For comparison, we also fabricated a controlled ZAB based on the MnO/NC-600 catalyst, denoted as MnO/NC-600-ZAB. As depicted in Fig. 6a, MnO/NC-900-ZAB exhibits a higher open-circuit voltage (1.39 V) compared to MnO/NC-600-ZAB (1.37 V), indicating its enhanced discharge capability. Fig. 6b presents

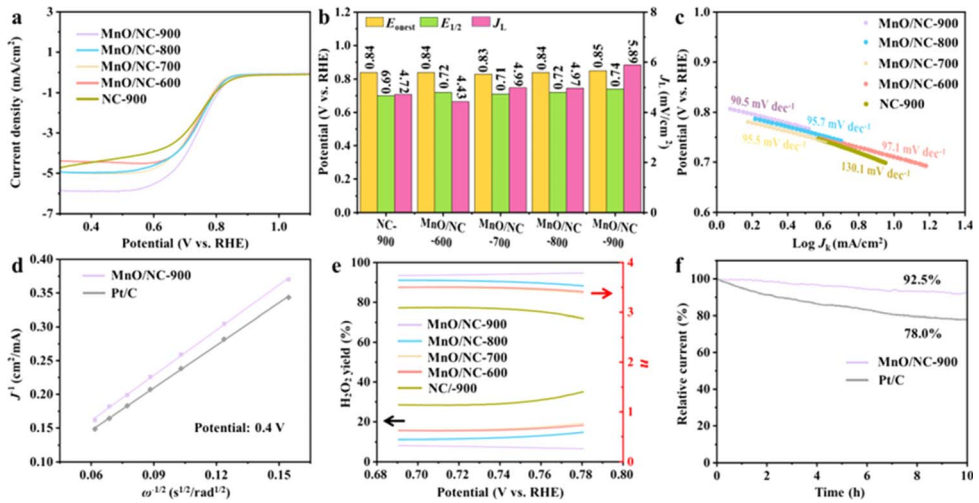

Fig. 5 ORR performance of MnO/NC nanohybrids and NC-900: (a) LSV curves in O_2-saturated 0.1 M KOH at 5 mV s^{-1}; (b) E_{onset}, $E_{1/2}$ and J_L values; (c) Tafel plots derived from the corresponding LSVs. (d) K–L plots of MnO/NC-900 and Pt/C at 0.4 V. (e) H_2O_2 yield and n of MnO/NC nanohybrids and NC-900. (f) Chronoamperometric tests of MnO/NC-900 and Pt/C in O_2-saturated KOH (0.1 M).

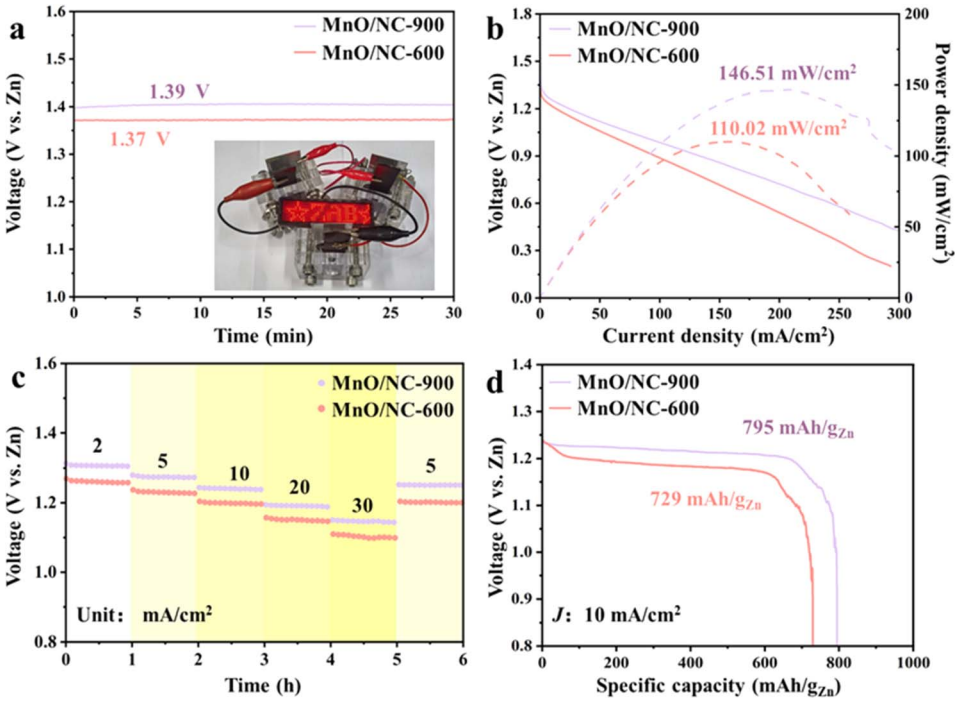

Fig. 6 Electrochemical performance of MnO/NC-600-ZAB and MnO/NC-900-ZAB. (a) Open-circuit voltage plot (inset shows the photograph of an LED screen powered by three MnO/NC-900-ZAB cells in series); (b) discharge polarization curves and corresponding power density curves; (c) discharge voltage retention at various current densities; (d) discharge curves at 10 mA cm^{-2}.

the discharge polarization curves and corresponding power density for these two ZABs. Clearly, MnO/NC-900-ZAB shows higher voltage output than MnO/NC-600-ZAB under the same current density. Additionally, MnO/NC-900-ZAB achieves a maximum power density of 146.5 mW cm^{-2}, surpassing that of MnO/NC-600-ZAB (110.0 mW cm^{-2}). The discharge voltage retention at diverse current densities (2–30 mA cm^{-2}) was evaluated (Fig. 6c). As shown, the potentials of MnO/NC-900-ZAB and MnO/NC-600-ZAB recover well but slightly decrease when the current density is reset to 5 mA cm^{-2}. Moreover, all discharge voltages of MnO/NC-900-ZAB are larger than those of MnO/NC-600-ZAB. At a current density of 10 mA cm^{-2}, MnO/NC-900-ZAB delivers a specific capacity of 795 mA h g_{Zn}^{-1} (Fig. 6d), significantly outperforming MnO/NC-600-ZAB (729 mA h g_{Zn}^{-1}). More importantly, MnO/NC-900-ZAB achieves an excellent high-rate discharge performance: it retains large specific capacity values when increasing the current density from 10 to 100 mA cm^{-2} (Fig. S11†). The cycling performance of MnO/NC-900-ZAB was measured by galvanostatic charge–discharge with per cycle being 10 min at a current density of 5 mA cm^{-2}. As revealed in Fig. S12,† the MnO/NC-900-ZAB initially shows a small charge–discharge gap (0.75 V) and unobvious voltage variation after 360 cycles (60 h) run, indicating its robust cycle life. The corresponding voltage efficiency is 61.5% initially and then drop to 58.2% at the 360th cycle. Furthermore, three MnO/NC-900-ZAB devices connected in series can light up a 3.0 V LED screen (inset of Fig. 6a). The superior electrochemical performance of MnO/NC-900-ZAB indicates MnO/NC-900 electrode exhibits the reduced mass diffusion barrier, thus effectively improving the accessibility of electrolyte and O_2 to the three-phase reaction region in the cathode.[42,47,48] Based on the above discussion, the MnO/NC-900 has the great potential to be applied in the metal–air batteries field.

4. Conclusion

We have developed a series of ORR catalysts by anchoring MnO nanoparticles on NC *via* a facile hydrothermal and pyrolytic process. The pyrolysis temperature had a great influence on the ORR activities of MnO/NC samples. Among them, the optimized catalyst, MnO/NC-900, demonstrated exceptional ORR performance in KOH electrolyte, surpassing other MnO/NC samples and NC-900. Furthermore, MnO/NC-900 exhibited the excellent ORR stability that was even superior to Pt/C. This heightened activity was primarily owing to the synergistic effect between MnO and NC, along with plentiful of surface carbon defects and surface-active compositions. When employed as the cathodic catalyst in ZAB, our designed MnO/NC-900 electrode exhibited an efficient ZAB behavior, including a high peak power density (146.5 mW cm^{-2}) and a large specific capacity (795 mA h g_{Zn}^{-1}), and a long cycling performance up to 60 h. Our study offers a pathway for the rational design of hybrid structures of non-precious metal materials to enhance ORR performance in metal–air batteries.

Data availability

All data that support the findings of this study are included within the article (and any ESI† files).

Author contributions

Qingxi Zhuang: investigation, data curation, validation, writing – original draft, writing – review and editing; Chengjun Hu: investigation, data curation, validation, writing – original draft; Weiting Zhu: writing – original draft; Gao Cheng: conceptualization, supervision, writing – original draft, writing – review & editing, funding acquisition; Meijie Chen: methodology, data curation; Ziyuan Wang: funding acquisition; Shijing Cai: writing – original draft; Litu Li: Methodology; Zier Jin: resources, writing – original draft, funding acquisition. Qiang Wang: supervision, writing – original draft, writing – review & editing.

Conflicts of interest

There are no conflicts to declare in our work.

Acknowledgements

This work was financially supported by the Foundation of Basic and Applied Basic Research of Guangdong Province (2023B1515120043) and Science and Technology Program of Guangzhou (202201010373). The authors also thank the technical support provided by the Analysis and Test Center of the Guangdong University of Technology.

References

1 A. Kondori, M. Esmaeilirad, A. M. Harzandi, R. Amine, M. T. Saray, L. Yu, T. C. Liu, J. G. Wen, N. N. Shan, H.-H. Wang, A. T. Ngo, P. C. Redfern, C. S. Johnson, K. Amine, R. Shahbazian-Yassar, L. A. Curtiss and M. Asadi, A room temperature rechargeable Li_2O-based lithium-air battery enabled by a solid electrolyte, *Science*, 2023, **379**, 6631.

2 X. R. Chen, J. Venezuela, Z. M. Shi, L. Z. Wang and M. Dargusch, Ultra-high-purity Mg-Ge anodes enable a long-lasting, high energy-density Mg-air battery, *Nano Energy*, 2024, **122**, 109269.

3 S. W. Ning, M. Li, X. Wang, X. Wang, D. Zhang, B. Y. Zhang, C. K. Wang, D. M. Sun, Y. W. Tang, H. Li, K. Sun and G. T. Fu, Importing antibonding-orbital occupancy through Pd-O-Gd bridge promotes electrocatalytic oxygen reduction, *Angew. Chem., Int. Ed.*, 2023, **62**(52), e202314565.

4 X.-W. Lv, Z. L. Wang, Z. Z. Lai, Y. P. Liu, T. Y. Ma, J. X. Geng and Z.-Y. Yuan, Rechargeable zinc–air batteries: advances, challenges, and prospects, *Small*, 2023, **20**(4), 2306396.

5 W. Yan, X. Wang, M. M. Liu, K. Y. Ma, L. Q. Wang, Q. C. Liu, C. K. Wang, X. Jiang, H. Li, W. Y. Tang and G. T. Fu, PCTS-controlled synthesis of $L1_0$/$L1_2$-typed Pt-Mn intermetallics for electrocatalytic oxygen reduction, *Adv. Funct. Mater.*, 2023, **34**(6), 2310487.

6 H. X. Yuan, W. Gao, X. H. Wan, J. Q. Ye, F. Y. Ma and D. Wen, Surface engineering of Pt aerogels by metal phthalocyanine to enhance the electrocatalytic property for oxygen reduction reaction, *Mater. Today Energy*, 2023, **37**, 101379.

7 T. Butburee, J. Ponchai, P. Khemthong, P. Mano, P. Chakthranont, S. Youngjan, J. Phanthasri, S. Namuangruk, K. Faungnawakij, X. Y. Wang, Y. Chen and L. J. Zhang, General pyrolysis for high-loading transition metal single atoms on 2D-nitro-oxygenous carbon as efficient ORR electrocatalysts, *ACS Appl. Mater. Interfaces*, 2024, **16**(8), 10227–10237.

8 X. Wang, Y. W. Tang, J.-M. Lee and G. T. Fu, Recent advances in rare-earth-based materials for electrocatalysis, *Chem Catal.*, 2022, **2**(5), 967–1008.

9 H. F. Xu, Z. Z. Ma, Z. H. Wan, Z. An and X. G. Wang, Recent advances and prospects of iron-based noble metal-free catalysts for oxygen reduction reaction in acidic environment: a mini review, *Int. J. Hydrogen Energy*, 2024, **59**, 697–714.

10 X. Wang, M. Li, P. Wang, D. M. Sun, L. F. Ding, H. Li, Y. W. Tang and G. T. Fu, Spin-selective coupling in mott-Schottky Er_2O_3-Co boosts electrocatalytic oxygen reduction, *Small Methods*, 2023, **7**(7), 2300100.

11 N. F. H. N. Zaiman and N. Shaari, Review on flower-like structure nickel based catalyst in fuel cell application, *J. Ind. Eng. Chem.*, 2023, **119**, 1–76.

12 K. B. Ibrahim, M.-C. Tsai, S. A. Chala, M. K. Berihun, A. W. Kahsay, T. A. Berhe, W.-N. Su and B.-J. Hwang, A review of transition metal-based bifunctional oxygen electrocatalysts, *J. Chin. Chem. Soc.*, 2019, **66**(8), 829–865.

13 F. Yang, X. Y. Gao, J. H. Xie, X. Q. Liu, J. X. Jiang and X. H. Lu, Cobalt-based electrocatalysts as air cathodes in rechargeable Zn-air batteries: advances and challenges, *Small Struct.*, 2021, **2**(12), 2100144.

14 X. Y. Zheng, A. M. Zuria and M. Mohamedi, Hybrid carbon sphere chain-MnO_2 nanorods as bifunctional oxygen electrocatalysts for rechargeable zinc–air batteries, *Inorg. Chem.*, 2023, **62**(2), 989–1000.

15 G. T. Fu, X. X. Yan, Y. F. Chen, L. Xu, D. M. Sun, J.-M. Lee and Y. W. Tang, Boosting bifunctional oxygen electrocatalysis with 3D graphene aerogel-supported Ni/MnO particles, *Adv. Mater.*, 2017, **30**(5), 1704609.

16 Y.-C. Zhang, S. Ullah, R. R. Zhang, L. Pan and X. W. Zhang, Manipulating electronic delocalization of Mn_3O_4 by manganese defects for oxygen reduction reaction, *Appl. Catal., B*, 2020, **277**, 119247.

17 Q. L. Wu, M. L. Jiang, X. F. Zhang, J. N. Cai and S. Lin, A novel octahedral MnO/RGO composite prepared by thermal decomposition as a noble-metal free electrocatalyst for ORR, *J. Mater. Sci.*, 2017, **52**, 6656–6669.

18 Y. M. Tan, C. F. Xu, G. X. Chen, X. L. Fang, N. F. Zheng and Q. J. Xie, Facile synthesis of manganese-oxide-containing mesoporous nitrogen-doped carbon for efficient oxygen reduction, *Adv. Funct. Mater.*, 2012, **22**, 4584–4591.

19 D. Guo, S. Dou, X. Li, J. T. Xu, S. Y. Wang, L. F. Lai, H. K. Liu, J. M. Ma and S. X. Dou, Hierarchical MnO_2/rGO hybrid nanosheets as an efficient electrocatalyst for the oxygen reduction reaction, *Int. J. Hydrogen Energy*, 2016, **41**(10), 5260–5268.

20 Q. M. Yu, J. X. Xu, C. X. Wu, J. S. Zhang and L. H. Guan, MnO_2 nanofilms on nitrogen-doped hollow graphene spheres as

a high-performance electrocatalyst for oxygen reduction reaction, *ACS Appl. Mater. Interfaces*, 2016, **8**(51), 35264–35269.

21 H. W. Shi, X. Yin, Y. N. Hua and Z. Gao, MnO nanoparticles loaded on three-dimensional N-doped carbon as highly efficient electrocatalysts for the oxygen reduction reaction in alkaline media, *Int. J. Hydrogen Energy*, 2022, **47**(47), 20507–20517.

22 T. W. Zhang, Z. F. Li, P. S, L. K. Wang, X. L. Niu and S. W. Wang, α-MnO_2 nanorods supported on three dimensional graphene as high activity and durability cathode electrocatalysts for magnesium-air fuel cells, *Catal. Today*, 2020, **355**, 304–310.

23 D. Mahato, A. Praveen, L. K. Nivedha, T. Gurusamy, K. Ramanujam, P. Haridoss and T. Thomas, Elucidating the role of interface of Cu-Co hybrid metal oxide for oxygen reduction reaction in Zn–air batteries, *Surf. Interfaces*, 2024, **46**, 103924.

24 F. Gu, W. G. Guo, Y. F. Yuan, Y.-P. Deng, H. L. Jin, J. C. Wang, Z. W. Chen, S. Pan, Y. H. Chen and S. Wang, External field-responsive ternary non-noble metal oxygen electrocatalyst for rechargeable zinc-air batteries, *Adv. Mater.*, 2024, **36**(19), 2313096.

25 J. S. Li, Z. Zhou, K. Liu, F. Z. Li, Z. G. Peng, Y. G. Tang and H. Y. Wang, Co_3O_4/Co-N-C modified Ketjenblack carbon as an advanced electrocatalyst for Al-air batteries, *J. Power Sources*, 2017, **343**, 30–38.

26 C. Li, X. P. Han, F. Y. Cheng, Y. X. Hu, C. C. Chen and J. Chen, Phase and composition controllable synthesis of cobalt manganese spinel nanoparticles towards efficient oxygen electrocatalysis, *Nat. Commun.*, 2015, **6**, 7345.

27 J. Y. Chen, J. Guo, H. Zhong, D. J. L. Brett and S. Gadipelli, Efficient electrocatalytic oxygen reduction reaction of thermally optimized carbon black supported zeolitic imidazolate framework nanocrystals under low-temperature, *RSC Adv.*, 2023, **13**, 34556.

28 G. Cheng, G. L. Liu, P. Liu, L. Y. Chen, S. B. Han, J. X. Han, F. Ye, W. Song, B. Lan, M. Sun and L. Yu, Nitrogen-doped Ketjenblack carbon supported Co_3O_4 nanoparticles as a synergistic electrocatalyst for oxygen reduction reaction, *Front. Chem.*, 2019, **7**, 766.

29 K. X. Ding, J. G. Hu, J. Luo, W. Jin, L. M. Zhao, L. R. Zheng, W. S. Yan, B. C. Weng, H. S. Hou and X. B. Ji, Confined N-$CoSe_2$ active sites boost bifunctional oxygen electrocatalysis for rechargeable Zn-air batteries, *Nano Energy*, 2022, **91**, 106675.

30 C. Sun, T. Chen, Q. X. Huang, X. G. Duan, M. X. Zhan, L. J. Ji, X. D. Li, S. B. Wang and J. H. Yan, Biochar cathode: reinforcing electro-fenton pathway against four-electron reduction by controlled carbonization and surface chemistry, *Sci. Total Environ.*, 2021, **754**, 142136.

31 H. Q. Liu, D. X. Hua, R. Wang, Z. G. Liu, J. J. Li, X. J. Wang and B. Song, High-performance bifunctional oxygen electrocatalysts for zinc–air batteries over nitrogen-doped carbon encapsulating CoNi nanoparticles, *J. Phys. D: Appl. Phys.*, 2022, **55**(48), 484005.

32 Q. Liu, P. Z. Qiao, M. M. Tong, Y. Xie, X. X. Zhang, K. Lin, Z. J. Liang, L. Wang and H. G. Fu, Enhancing zinc–air battery performance by constructing three-dimensional N-doped carbon coating multiple valence Co and MnO heterostructures, *Nano Res.*, 2024, **17**, 5104–5113.

33 L. X. Wang, J. Huang, X. R. Hu, Z. Y. Huang, M. C. Gao, D. Yao, T. T. Isimjan and X. L. Yang, Synergistic vacancy engineering of Co/MnO@NC catalyst for superior oxygen reduction reaction in liquid/solid zinc–air batteries, *J. Colloid Interface Sci.*, 2024, **660**, 989–996.

34 C. Q. Shang, M. Y. Yang, Z. Y. Wang, M. C. Li, M. Liu, J. Zhu, Y. G. Zhu, L. J. Zhou, H. Cheng, Y. Y. Gu, Y. G. Tang, X. Z. Zhao and Z. G. Lu, Encapsulated MnO in N-doping carbon nanofibers as efficient ORR electrocatalysts, *Sci. China Mater.*, 2017, **60**(10), 937–946.

35 Z. Y. Du, P. Yu, L. Wang, C. G. Tian, X. Liu, G. Y. Zhang and H. G. Fu, Cubic imidazolate frameworks-derived CoFe alloy nanoparticles-embedded N-doped graphitic carbon for discharging reaction of Zn-air battery, *Sci. China Mater.*, 2019, **63**(3), 327–338.

36 Q. Y. Jin, B. W. Ren, J. P. Chen, H. Cui and C. X. Wang, A facile method to conduct 3D self-supporting Co-FeCo/N-doped graphene-like carbon bifunctional electrocatalysts for flexible solid-state zinc air battery, *Appl. Catal., B*, 2019, **256**, 117887.

37 X. D. Duan, M. Q. Xia, X. X. Hu, L. J. Yang and H. G. Zheng, Interfacing MnO and FeCo alloy inside N-doped carbon hierarchical porous nanospheres derived from metal–organic framework to boost high-performance oxygen reduction for Zn-air batteries, *Nanoscale*, 2022, **14**(44), 16516–16523.

38 S. B. Han, Y. Wu, S. M. Peng, Y. Y. Xu, M. Sun, X. H. Su, Y. H. Zhong, H. L. Wen, J. He and L. Yu, Boosting the electrochemical performance of Zn-air battery with N/O co-doped biochar catalyst *via* a simple physical strategy of forced convection intensity, *Chem. Eng. Sci.*, 2023, **272**, 118615.

39 H. X. Sun, P. L. Zhou, X. Y. Ye, J. J. Wang, Z. Y. Tian, Z. Q. Zhu, C. H. Ma, W. D. Liang and A. Li, Nitrogen-doping hollow carbon nanospheres derived from conjugated microporous polymers toward oxygen reduction reaction, *J. Colloid Interface Sci.*, 2022, **617**, 11–19.

40 M. G. Wang, F. Peng, M. Wang and J. Han, N-doped carbon nanospheres with nanocavities to encapsulate manganese oxides as ORR electrocatalysts, *New J. Chem.*, 2020, **44**(35), 14915–14921.

41 Q. C. Wang, Y. J. Ji, Y. P. Lei, Y. B. Wang, Y. D. Wang, Y. Y. Li and S. Y. Wang, Pyridinic-N-dominated doped defective graphene as a superior oxygen electrocatalyst for ultrahigh-energy-density Zn-air batteries, *ACS Energy Lett.*, 2018, **3**(5), 1183–1191.

42 Q. Zhou, S. Miao, T. Xue, Y. P. Liu, H. Li, X.-H. Yan, Z.-L. Zou, B.-P. Wang, Y.-J. Lu and F.-L. Han, Nitrogen-doped porous carbon encapsulates multivalent cobalt-nickel as oxygen reduction reaction catalyst for zinc–air battery, *J. Colloid Interface Sci.*, 2023, **648**, 511–519.

43 F. Li, T. T. Qin, Y. P. Sun, R. J. Jiang, J. F. Yuan, X. Q. Liu and A. P. O'Mullane, Preparation of a one-dimensional hierarchical MnO@CNT@Co-N/C ternary nanostructure as a high-performance bifunctional electrocatalyst for rechargeable Zn-air batteries, *J. Mater. Chem. A*, 2021, **9**, 22533–22543.

44 X. F. Lu, Y. Chen, S. B. Wang, S. Y. Gao and X. W. Lou, Interfacing manganese oxide and cobalt in porous graphitic carbon polyhedrons boosts oxygen electrocatalysis for Zn-air batteries, *Adv. Mater.*, 2019, **31**(39), 1902339.

45 J. Z. Zou, T. Liang, M. G. Peng, P. Liu, Z. Li, J. M. Wen, Z. J. Li, Y. S. Yan, X. Yu, X. R. Zeng and J. F. Huang, Construction of oxygen-vacancy-rich 2D nitrogen-doped carbon nanosheets with CoFe@$CoFe_2O_4$ heterogeneous interfacial structure for rechargeable Zn-air batteries, *J. Energy Storage*, 2024, **84**, 110815.

46 H. Li, G. Y. Wu, G. J. Cheng, Y. Shuai, S. C. Liu and Y. Liu, CoNi nanoalloys embedded in N-doped carbon nanofibers derived from layered bimetal–organic framework and as efficient oxygen electrocatalyst, *J. Alloys Compd.*, 2021, **888**, 161588.

47 P. Xu, W. Chen, Q. Wang, T. Zhu, M. Wu, J. Qiao, Z. Chen and J. Zhang, Effects of transition metal precursors (Co, Fe, Cu, Mn, or Ni) on pyrolyzed carbon supported metal–aminopyrine electrocatalysts for oxygen reduction reaction, *RSC Adv.*, 2015, **5**, 6195–6206.

48 M. K. Aslam, H. Wang, S. Chen, Q. Li and J. Duan, Progress and perspectives of metal (Li, Na, Al, Zn and K)-CO_2 batteries, *Mater. Today Energy*, 2023, **31**, 101196.